REPORT DOCUMENTATION PAGE

1. REPORT DATE *(DD-MM-YYYY)* 13-10-2011	2. REPORT TYPE Conference Paper	3. DATES COVERED *(From - To)*

4. TITLE AND SUBTITLE

Proper Orthogonal Decomposition Analysis of Shear-Coaxial Injector Flows with and Without Transverse Acoustic Forcing

5a. CONTRACT NUMBER

5b. GRANT NUMBER

5c. PROGRAM ELEMENT NUMBER

6. AUTHOR(S)

Sophonias Teshome, Ivett Leyva and Douglas Talley

5d. PROJECT NUMBER

5f. WORK UNIT NUMBER
23080533

7. PERFORMING ORGANIZATION NAME(S) AND ADDRESS(ES)

Air Force Research Laboratory (AFMC)
AFRL/RZSA
10 E. Saturn Blvd.
Edwards AFB CA 93524-7680

8. PERFORMING ORGANIZATION REPORT NUMBER

AFRL-RZ-ED-TP-2011-402

9. SPONSORING / MONITORING AGENCY NAME(S) AND ADDRESS(ES)

Air Force Research Laboratory (AFMC)
AFRL/RZS
5 Pollux Drive
Edwards AFB CA 93524-7048

10. SPONSOR/MONITOR'S ACRONYM(S)

11. SPONSOR/MONITOR'S NUMBER(S)

AFRL-RZ-ED-TP-2011-402

12. DISTRIBUTION / AVAILABILITY STATEMENT

Approved for public release; distribution unlimited (PA #11875).

13. SUPPLEMENTARY NOTES
For presentation at the JANNAF 2011 Joint Subcommittee Meeting, Huntsville, AL, 5-9 Dec 2011.

14. ABSTRACT

This experimental study investigated the response of dynamic flow structures of cryogenic coaxial nitrogen jets to pressure perturbations due to transverse acoustic forcing at a pressure antinode (PAN). The role of injector exit geometry on the flow response was examined using two shear coaxial injectors with different outer-to-inner jet area ratios. Flow conditions spanning subcritical (reduced pressure of 0.44) to supercritical (reduced pressure of 1.05) chamber pressures, varying outer-to-inner jet momentum flux ratios (0.5 – 20), and acoustic pressure antinode at the jet axis location were considered. A basic application of proper orthogonal decomposition on the intensity fluctuation of high-speed images enabled the extraction of the spatial and temporal characteristics of the dominant flow structures that existed in the flow field during exposure to acoustic forcing. Regardless of injector geometry or pressure regime, low outer-to-inner momentum flux ratio flows were found to be responsive to acoustic pressure antinode forcing. With increasing momentum flux ratio, however, the flow response to forcing depended on the injector geometry.

15. SUBJECT TERMS

16. SECURITY CLASSIFICATION OF:			17. LIMITATION OF ABSTRACT	18. NUMBER OF PAGES	19a. NAME OF RESPONSIBLE PERSON Dr. Douglas Talley
a. REPORT Unclassified	b. ABSTRACT Unclassified	c. THIS PAGE Unclassified	SAR	18	19b. TELEPHONE NUMBER *(include area code)* N/A

PROPER ORTHOGONAL DECOMPOSITION ANALYSIS OF SHEAR-COAXIAL INJECTOR FLOWS WITH AND WITHOUT TRANSVERSE ACOUSTIC FORCING

S. Teshome[†], I. A. Leyva[‡], D. Talley[‡]
[†]University of California, Los Angeles, Los Angeles, CA
[‡]Air Force Research Laboratory, Edwards AFB, CA

ABSTRACT

This experimental study investigated the response of dynamic flow structures of cryogenic coaxial nitrogen jets to pressure perturbations due to transverse acoustic forcing at a pressure antinode (PAN). The role of injector exit geometry on the flow response was examined using two shear coaxial injectors with different outer-to-inner jet area ratios. Flow conditions spanning subcritical (reduced pressure of 0.44) to supercritical (reduced pressure of 1.05) chamber pressures, varying outer-to-inner jet momentum flux ratios (0.5 – 20), and acoustic pressure antinode at the jet axis location were considered. A basic application of proper orthogonal decomposition on the intensity fluctuation of high-speed images enabled the extraction of the spatial and temporal characteristics of the dominant flow structures that existed in the flow field during exposure to acoustic forcing. Regardless of injector geometry or pressure regime, low outer-to-inner momentum flux ratio flows were found to be responsive to acoustic pressure antinode forcing. With increasing momentum flux ratio, however, the flow response to forcing depended on the injector geometry.

NOMENCLATURE

A area
D diameter
f frequency
J outer jet-to-inner jet momentum flux ratio, $\rho_2 U_2^2/\rho_1 U_1^2$
m no. of columns of pixels in a single image frame
$\dot{m}$ mass flow rate
N no. of image frames
n no. of rows of pixels in a single image frame
P pressure
Pr reduced pressure, P/P_{cr}
R outer-to-inner jet velocity ratio, U_2/U_1
Re Reynolds number
S outer-to-inner jet density ratio, ρ_2/ρ_1
T temperature
U flow velocity

GREEK SYMBOLS

θ shear-layer momentum thickness
ρ density

SUBSCRIPTS

1,2   pertaining to the inner jet, outer jet, respectively
F   acoustically forced

I. INTRODUCTION

Coaxial injectors have proven to be one of the most effective and simple means of delivering propellants in combustion devices such as in liquid rocket engines (LREs). Their application in LREs was seen as early as the development of the J-2 engine and as recent as the space shuttle main engine (SSME). Combustion instability is a phenomenon that has, in severe instances, led to the demise of LREs. It is primarily a result of feedback interactions

between unsteady combustion rates and pressure fluctuations from acoustic modes in the combustion chamber. Since injector flows are directly involved in processes that take place inside combustors, it is crucial to understand how they contribute to, as well as how they are affected by, these unsteady physical mechanisms that lead to combustion instabilities. However, a successful understanding at a fundamental level of these interactions between injector flows and chamber phenomena can only be achieved by first isolating the fluid dynamics aspect from the reactive flow processes, and studying the coupling of non-reactive injector flow instabilities with external pressure perturbations.

Shear-coaxial jets consist of a circular core or inner jet and an annular or outer jet. In the near field region, where the potential cores of both the inner and outer jets exist, two shear-layers exist: an inner shear layer between the inner and outer jet flow, and an outer shear layer between the outer jet and the ambient fluid. Detailed descriptions and characteristics of the different flow regimes in coaxial jets are given, for example, in [1]. The development of instabilities in the individual shear layers, and the interaction between the two shear layers has a direct impact on the eventual instability characteristics of the entire flow field. Several studies [2-5] investigate the existence and behavior of large-scale vortex structures in the near-field region of single-phase similar or different density coaxial jets. It was shown that for outer jet velocity (U_2) to inner jet velocity (U_1) ratios exceeding unity ($R = U_2/U_1 > 1$), coherent structures in the outer shear layer dominate those in the inner shear layer.

The influence of these coherent structures on the overall dynamics of the flow field calls for an understanding of the factors leading to their formation. Detailed studies on the development and growth of natural instabilities in a single circular jet [6] or a single circular jet with coflow [7] reveal two of the most significant natural modes of instability: the axisymmetric and the first azimuthal or helical modes. These modes have comparable amplification rates over most of the core region downstream of the exit, with the helical mode eventually dominating the flow field farther downstream. It is shown [1] that the development of the outer shear layer of a coaxial jet behaves as the shear layer of a single jet, while the development of the inner shear layer behaves as that of a single jet issuing into an external flow. Thus, the axisymmetric and helical modes of instability along with natural as well as externally imposed flow conditions, such as pressure or velocity perturbations, that affect their development may be used to assess the stability of the coaxial jet.

The present study continues the series of experimental studies done in the same facility [8-14], which looked at the behavior of shear-coaxial N_2 jets at elevated pressures with and without the presence of a transverse acoustic field. It examines the baseline flow characteristics of two injectors with similar inner jet post thickness to diameter ratio, but different outer jet to inner jet area ratios, for different momentum flux ratios. It also investigates the flow response to a pressure antinode forcing condition, where the coaxial jet is exposed to the maximum local pressure fluctuations in a transverse acoustic field. Unlike previous studies in the current facility, the present study applies a proper orthogonal decomposition (POD) analysis (see Section II) to reduce the information obtained from a set of high-speed back-lit images in order to characterize the spatial and temporal behavior of dominant flow structures in the inner shear layer of the baseline and acoustically forced flows. Using this novel approach, the goal is to gain a better understanding of the evolution of flow instabilities, and underline the critical differences in the flow stability characteristics brought about as a result of simple design alterations in the shear-coaxial injector.

II. EXPERIMENTAL SETUP AND METHODOLOGY

These experiments were carried out at the Air Force Research Laboratory (AFRL), Edwards, test cell EC-4. Figure 1 shows a schematic of the experimental facility. The chamber was designed to operate at pressures spanning subcritical to supercritical pressures of N_2, whose critical pressure is 3.4 MPa, and critical temperature is 126 K.
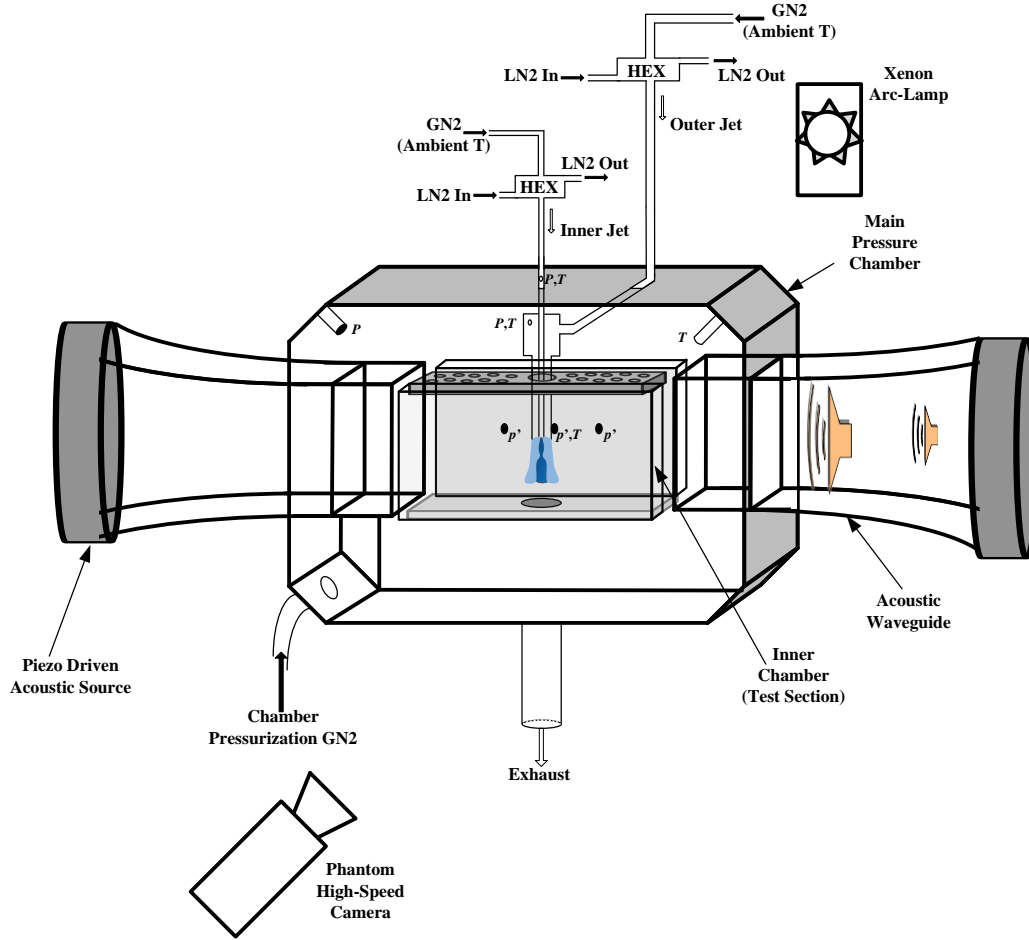
Figure 1. Experimental Facility Schematic

The inner and outer jets as well as the chamber pressurization flows were supplied by ambient temperature, high pressure facility GN2 lines. Counter-flow heat exchangers using LN2 as the coolant fluid were used to cool the test fluids down to the desired temperatures. An unshielded Omega type-E thermocouple with a bead diameter of 0.25 mm was mounted on top of two linear positioning stages and placed near the injector to measure the radial temperature profile of the coaxial jet within one inner jet diameter from the exit plane. Porter mass flow meters (model 123-DKASVDAA) were used to measure the inner and outer jet flow rates, which were controlled via metering valves. The jets issued into the test section (Figure 1) of the inner chamber halfway between the two piezo-sirens located at opposite ends of the chamber. Each piezo-siren was fitted with a waveguide that transitioned from a circular cross-section to a rectangular one. The inner chamber was used to maximize the amplitude of acoustic oscillations generated by the piezo-sirens. However, both the inner and main chambers were maintained at the same static pressure, which was measured with a Stellar ST1500 pressure transducer. The momentum flux ratio ($J = \rho_2 U_2^2/\rho_1 U_1^2$), velocity ratio ($R=U_2/U_1$), and other flow conditions were determined based on thermophysical properties evaluated at the measured chamber pressure, and jet exit temperatures. Kulite absolute (CCQ-093) and differential (XCQ-093, XCE-093) pressure transducers were also used for making high-speed acoustic pressure measurements. These pressure transducers were placed along the inner chamber wall, where one transducer was located directly behind the jet, and two others inside the injector plenums.

The acoustic wave signals were generated using a Fluke 292 arbitrary waveform generator. A Trek PZD2000A high-voltage amplifier amplified continuous sine wave signals from the waveform generator before being input into each piezo-siren. The resulting acoustic waves from each piezo-siren were traveling waves that propagated transversely along the waveguide. Depending on the phase difference between the signals applied to each piezo-siren, a pressure antinode (PAN) condition, where the perturbation in pressure was maximum, or a pressure node (PN) condition, where the perturbation in pressure was minimum, can be created. Thus, using signals

that were in-phase (0° phase difference), a PAN condition was established at the center of the waveguide, where the coaxial jets were situated.

Figure 2 shows a schematic of the injector exit with dimensional nomenclature, and Table 1 provides a summary of the injector exit dimensions under consideration. Both injectors were characterized by small lip thickness to inner diameter ratio t/D_1, but one had a large outer-to-inner jet cross-sectional area ratio (LAR), while the other had a small area ratio (SAR).

<div align="center">(a)   (b)   (c)</div>
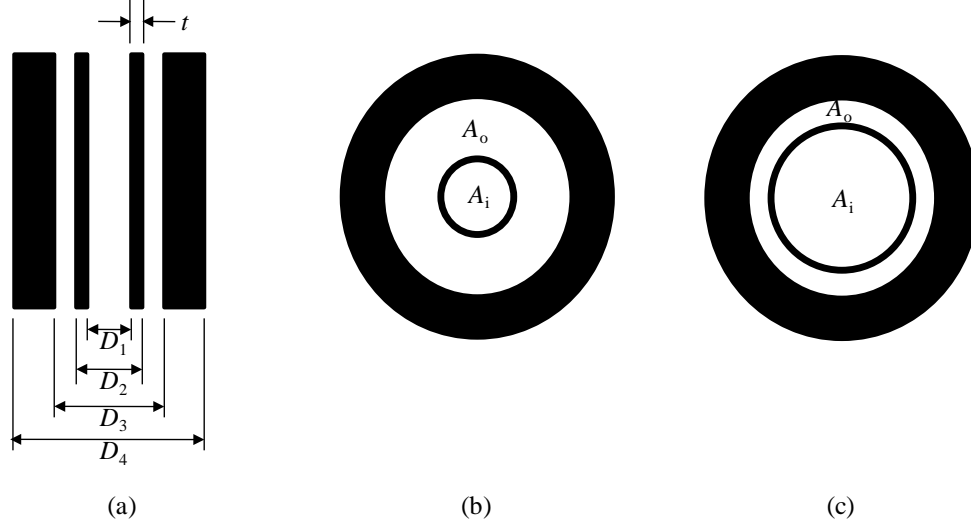
Figure 2. Injector geometry schematic: (a) axial cross-sectional view, (b) LAR exit configuration, (c) SAR exit configuration

<div align="center">Table 1. Injector Exit Dimensions (mm)</div>

Injector	t	D_1	t/D_1	D_2	D_3	D_4	A_o/A_i
LAR	0.09	0.70	0.13	0.89	2.44	3.94	10.6
SAR	0.13	1.40	0.09	1.65	2.44	3.94	1.65

Proper orthogonal decomposition (POD) of the high-speed images has proven to provide a powerful means for extracting relevant qualitative and quantitative information from an otherwise complicated and noise-ridden set of image data [15-17]. A xenon arc lamp was used to provide a back-lit image of the coaxial jet, which was visualized using a high speed Phantom v7.1 CMOS camera at framing rates exceeding 20 kHz. The decomposition was achieved by first arranging all the pixel intensity values of all frames into a single array, whereby the pixel intensities from one frame occupied one row of the data array. Thus, a set of N consecutive frames, each of which had an n by m pixel resolution, constituted an N by n $\times$ m data array. The temporal mean of the data array was subtracted in order to eliminate the DC component of the intensity values. The method of singular value decomposition was implemented in MATLAB® using a built-in subroutine to represent the data array of intensity fluctuations as a matrix product of an N by N array of temporal amplitude coefficients and an N by n $\times$ m array of right singular column vectors, also known as proper orthogonal modes. The matrix product of the left singular vectors and the diagonal matrix of singular values formed the matrix of column vectors of the temporal amplitude coefficients. These modes were arranged in decreasing order of significance as dictated by the magnitude of the singular values of the decomposition.

<div align="center">

III. RESULTS AND DISCUSSION

</div>

The experiments done under subcritical (reduced pressure, $Pr = 0.44$) pressure conditions were such that the inner jet was in liquid phase, while the outer jet was in gas phase at temperatures well above the saturation

temperature of N_2. Under nearcritical (reduced pressure, $Pr = 1.05$) conditions, the inner jet temperatures were below the critical temperature, while that of the outer jet were well above the critical temperature, thereby resulting in a supercritical outer fluid. A test matrix containing all the flow conditions and parameters is given in Table 2 in the Appendix. As previously noted, for coaxial jets of different densities, J is one of the governing parameters of coaxial jet mixing. However, for a set of test conditions in a particular pressure regime, the outer-to-inner jet density ratio ($S = \rho_2/\rho_1$) was held approximately constant while R was varied. Thus, the variation in J in these studies resulted mainly due the variation in R only.

The remainder of this section will focus on results pertaining to the coaxial jet without any acoustic forcing and with acoustic forcing that created a PAN condition inside the acoustic waveguide where the jets were situated.

BASELINE (NO ACOUSTICS)

As the name implies, this condition merely reflects a state of the coaxial jet flow without any type of external flow disturbances present. It provides information on the main characteristics of the natural flow disturbances, as well as a basis condition against which an acoustically forced flow response can be compared.

Figure 3(a) shows a snapshot image for $J = 0.5$ at $Pr = 0.44$ using LAR. It shows a single frame out of a set of images recorded at 25,000 fps. Characteristic of low J flow [10,11,14] , it shows a long dark-core region spanning the region up to $20D_1$ downstream of the injector exit. It also has a relatively small spread angle, which is indicative of the slow spatial shear-layer development. These features are also evident in Figure 3(b), which is a temporal mean of each individual pixel over 1,000 frames. A distinct difference between the snapshot and average images can be clearly seen by the absence of any discrete flow structures emanating from the dark-core at the jet interface boundary in the average image. These structures, which appear to be at least spatially periodic in Figure 3(a), start forming by about $10D_1$. It is to be noted that the inner jet tube was not perfectly flush, but sticks out by about $0.2D_1$. This allowed for direct visual confirmation that inner jet injector tube was not disturbed by turbulent flow disturbances in the outer jet.
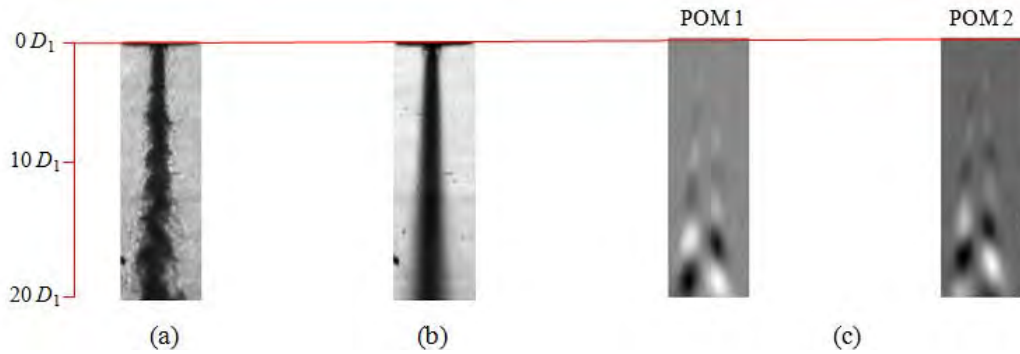

Figure 3. Baseline LAR flow at $Pr = 0.44$, $J = 0.5$: (a) snapshot image, (b) average image, (c) proper orthogonal mode (POM).

Figure 3(c) shows the first two proper orthogonal modes (POM) of the decomposition. As described in the previous section, since only the fluctuation in intensity level was considered, the background fluid and the relatively uniform portion of the inner jet flow were subtracted out, thus depicted by a gray region to indicate a mean level in a gray-scaled image. On the other hand, the lighter and darker lobes represent, respectively, the presence and absence of flow structures emanating from the dense inner jet. Their spatial arrangement is indicative of the symmetry or antisymmetry of the flow structures formed in the inner shear layer. That is, at any given axial location, the presence of two similar lobes adjacent to each other indicates the presence of flow structures associated with axisymmetric instabilities in the shear layer. Meanwhile, opposite adjacent lobes indicate antisymmetry, which in an axisymmetric flow geometry represents flow structures associated with helical instabilities. This is a viable assumption since under no external disturbances that can impose a preferential direction of oscillation of the shear-layer region, the only manner of propagation of the antisymmetric structures must be in the form of a helical disturbance. Hence, viewing

the jet from two perpendicular lines of sight should reveal indistinguishable features for a baseline coaxial jet, as was shown for some flow conditions in [8].

The singular values of all modes of the decomposition are shown in Figure 4. POMs 1 and 2 in Figure 3(c) whose singular values correspond to modes 1 and 2, respectively, are seen to be the two most dominant flow structures. Moreover, the monotonically decreasing magnitude of the singular values with increasing mode numbers, and more than an order of magnitude difference between the highest and lowest modes implies that the more important flow dynamics were captured by the lower mode numbers. This is actually a direct outcome of a POD procedure, which orders the singular values, and their corresponding POMs, in order of decreasing importance.
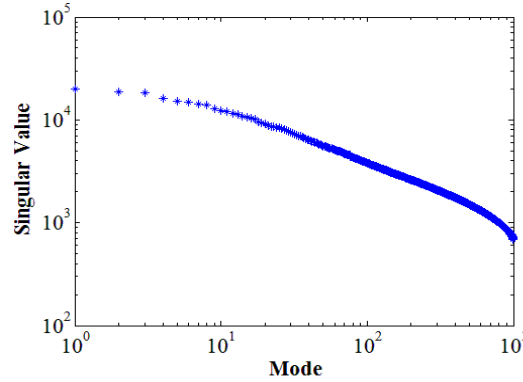
Figure 4. Baseline LAR flow at $Pr = 0.44$, $J = 0.5$: singular values.

The temporal characteristics of these dominant POMs were represented in the form of power spectral density of the temporal amplitude coefficients of the POD, and are shown in the plots in Figures 5(a, b). The peaks located at the low end of the spectra were associated with the disturbance frequencies of the lobes identified in their respective POMs. Furthermore, a time-sequence of images of each individual POM revealed a progression of changes in the lobe pattern similar to that of a standing wave. That is, with every passing period associated with the characteristic peak frequencies, a light lobe turned dark, and vice-versa. On the other hand, a time-sequence of images of a superposition of the two POMs revealed a continuous propagation of the lobes traveling downstream of the injector exit.

This outcome is analogous to a simply demonstrable result that the superposition of two standing one-dimensional waves is a traveling wave, as long as the two standing waves are $\pm 90^o$ out-of-phase both temporally and spatially. In a similar manner, the cross-power spectral density (CPSD) of the temporal amplitude coefficients can be used to check the existence of a phase difference of $\pm 90^o$ at the frequencies near the peak of a CPSD magnitude spectrum. Figures 5(c, d) show the CPSD magnitude and phase plots of POMs 1 and 2. The phase plot shows that the temporal requirement to form a propagating disturbance was satisfied by structures whose frequencies were associated with a -90° phase difference. It can thus be concluded that the frequencies associated with the peak in the CPSD magnitude plot were the characteristic frequencies of the propagating disturbances seen in the time sequence of the superposed POMs. A similar analysis demonstrating the spatial requirement for forming a propagating disturbance has not been done in the current study. However, it should be sufficient to check that the two POMs have similar lobe pattern, and together with the temporal requirement, form what are known as conjugate modes [16]. Hereafter, images of POMs presented will be the superposition of conjugate modes.

Figures 6(a-d) show the snapshot, average, and POM images for increasing J values at $Pr = 0.44$ using LAR. Figures 7(a-d) show similar images at $Pr = 1.05$. The decreasing dark-core lengths with increasing J are evident from both the snapshot and average images in both pressure regimes. In fact, it decreased from over $20D_1$ at $J = 0.5$ [Figures 3(a, b)] to less than $10D_1$ at $J = 20$ [Figure 6(d)], resulting in about 50% decrease at $Pr = 0.44$. The percent reduction was larger than 50% at $Pr = 1.05$ even at $J = 12$. This difference in the reduction is partly attributable to the transcritical state of the inner jet at $Pr = 1.05$, and the associated distinct physical properties, namely an almost non-existent surface tension and large momentum diffusivity. In either case, however, the dark-core length decrease very well signifies an increased rate of shear-layer growth, and thus enhanced mixing with

increasing *J* for this geometry. Although the end of the dark-core is not coincident with the end of the potential core, it is nevertheless a good

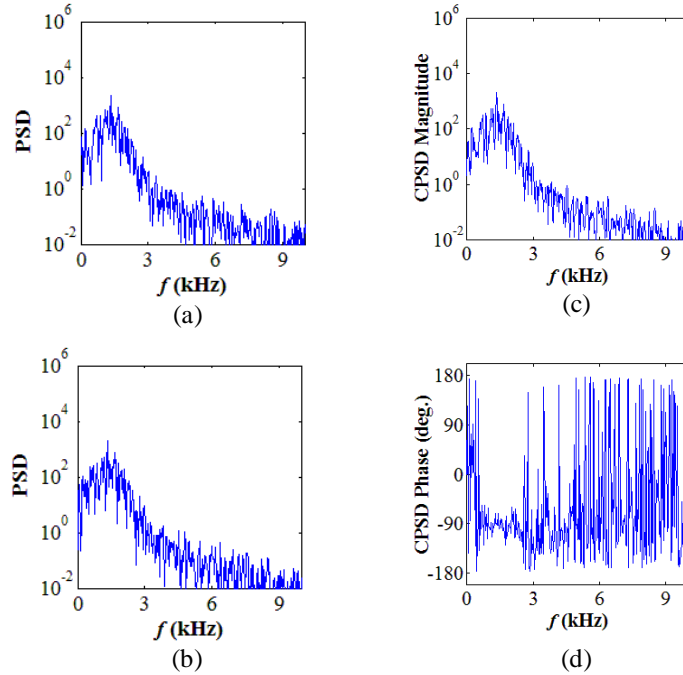Figure 5. Baseline LAR flow at $Pr = 0.44$, $J = 0.5$: power spectral density (PSD) of the temporal amplitude coefficients of the decomposition corresponding to (a) POM 1, (b) POM 2, and cross-power spectral density (CPSD) (c) magnitude, (d) phase.

The location downstream of the injector exit, where the helical disturbances begin to dominate the inner shear layer region also decreased with increasing *J*. This is in accordance with the well known progression of development of shear-layer instabilities in axisymmetric single or coaxial jets [6,7]. In the region close to the jet exit, where the shear-layer momentum thickness is very small compared to the jet diameter ($D/\theta >> 1$), all modes of instability have been shown to have the same growth rates, with the axisymmetric and helical instability growth rates remain significant and comparable while that of the others become negligible. At the end of the potential core, however, the growth rate of helical instabilities becomes the most prevalent. Therefore, what the POMs show may well be the helical mode of instability of the jet.

Figures 6(e-h) and Figures 7(e-h) show the corresponding CPSD magnitude spectra for increasing *J* values at $Pr = 0.44$ and $Pr = 1.05$, respectively. Clearly, the peak frequencies became broader and moved to higher frequencies as *J* increased. This behavior was in line with analytical results [7] that with increasing coflow velocity, the region of unstable frequencies becomes broader and that the peak of the spatial growth rates shift to higher frequencies. Another notable outcome from these spectra was that the peak frequencies were not dependent on *R* or *J*, but on the magnitude of the outer jet velocity. Despite the significant rise in *R* or *J* from Figure 6(g) to Figure 6(h), the peak for the latter sat at a slightly lower frequency than the former, since as shown in Table 2 in the Appendix, the magnitude of the outer velocity was smaller. However, further investigation will need to be done to generalize this outcome.

As described earlier, the only distinguishing design feature between LAR and SAR was A_o/A_i, where it was almost an order of magnitude smaller for the latter. Figures 8(a-d) and Figures 9(a, b) show similar snapshot, average and POM images for SAR at $Pr = 0.44$ and $Pr = 1.05$, respectively. At $Pr = 0.44$, it is evident that increasing *J* had a weaker influence on the dark-core length unlike for LAR. Due to the small hydraulic radius of the outer jet of SAR, the potential core of the outer jet was relatively short. Thus, an effective entrainment of the inner jet by the outer jet was limited to a relatively shorter distance from the exit plane. The influence of *J* on the dark-core length at $Pr = 1.05$ was more significant again due to the severely reduced to non-existent surface tension at the inner jet boundary.
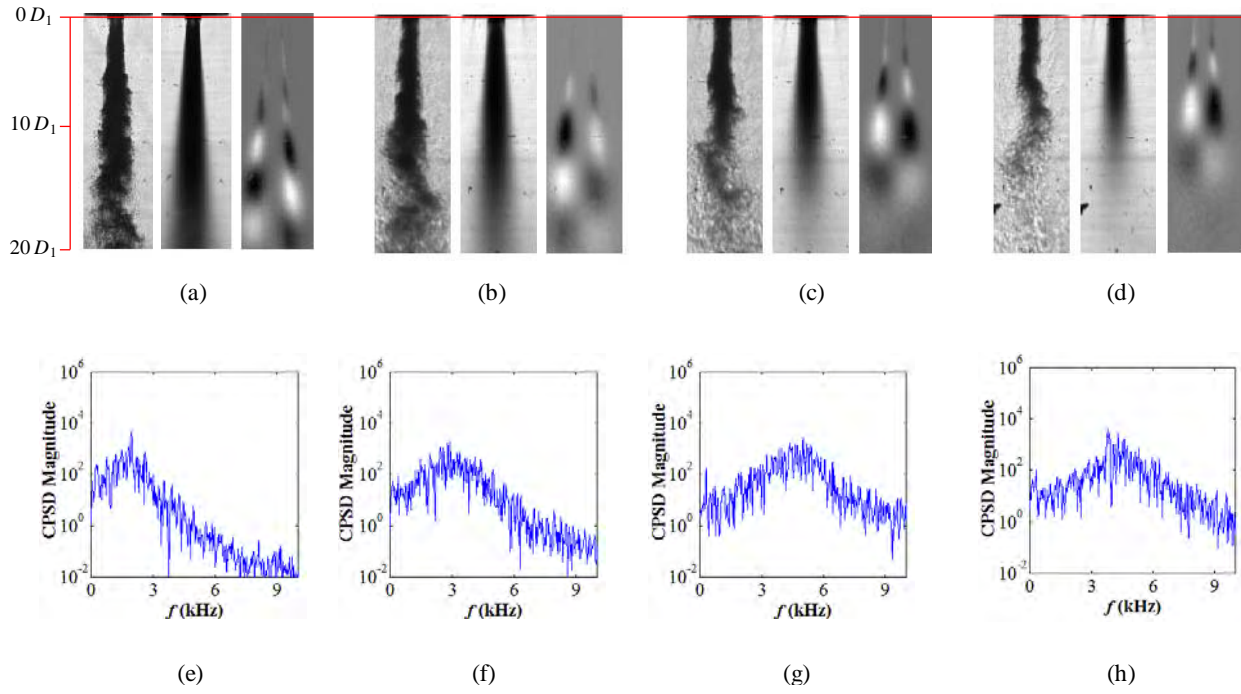
Figure 6. Baseline LAR flow at $Pr = 0.44$: snapshot, average, POM images for J (a) 2.1, (b) 5.2, (c) 11, (d) 20, and CPSD magnitude for J (e) 2.1, (f) 5.2, (g) 11, (h) 20.
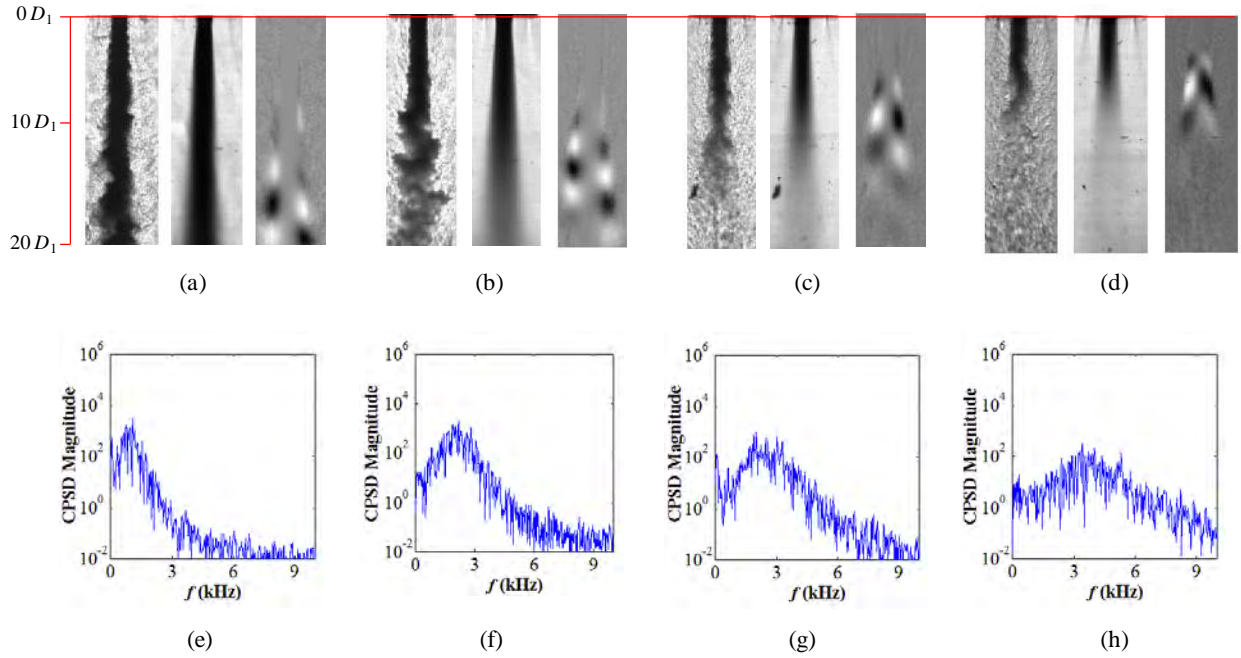

Figure 7. Baseline LAR flow at $Pr = 1.05$: snapshot, average, POM images for J (a) 0.5, (b) 1.9, (c) 5.0, (d) 12, and CPSD magnitude for J (e) 0.5, (f) 1.9, (g) 5.0, (h) 12.
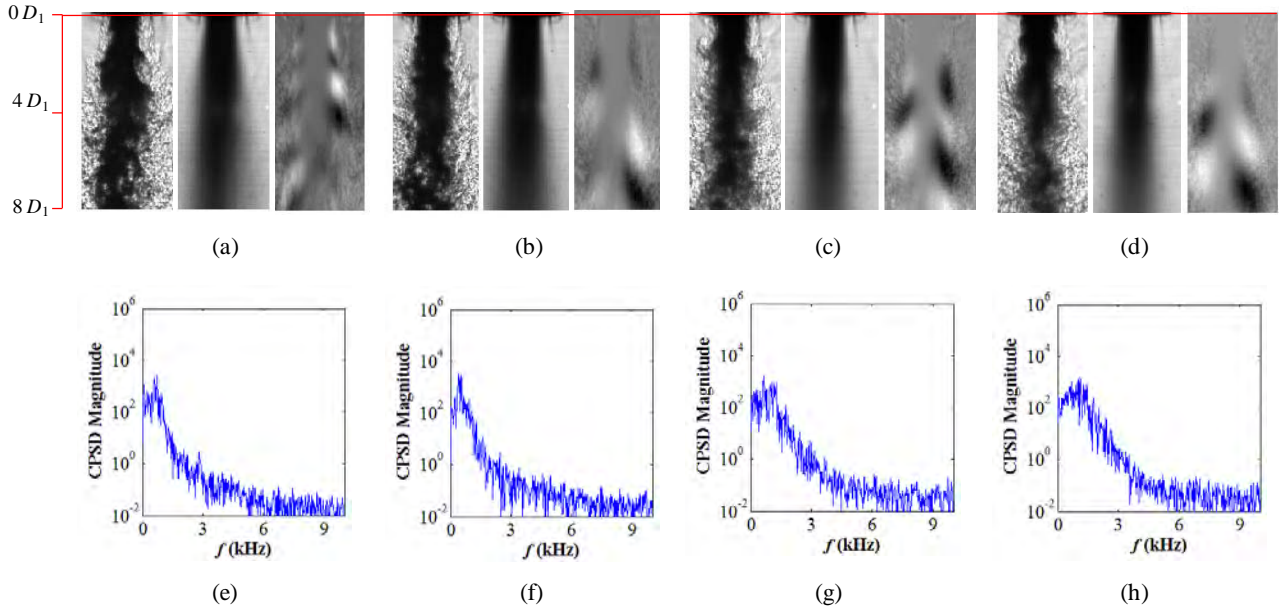
Figure 8. Baseline SAR flow at $Pr = 0.44$: snapshot, average, POM images for J (a) 2.0, (b) 5.2, (c) 12, (d) 17, and CPSD magnitude for J (e) 2.0, (f) 5.2, (g) 12, (h) 17.

The CPSD magnitude spectra in Figures 8(e-h) and Figures 9(c, d) show that the peak frequencies appear to be unaffected with increasing J values. This was in contradiction to the expected shift to higher frequencies and broadening of the range of peak frequencies as demonstrated by [7] for an increasing coflow velocity. The reason behind this may again be explained by how soon the inner and outer jets attain a single jet behavior, thereby rendering the effect of coflow nonexistent.
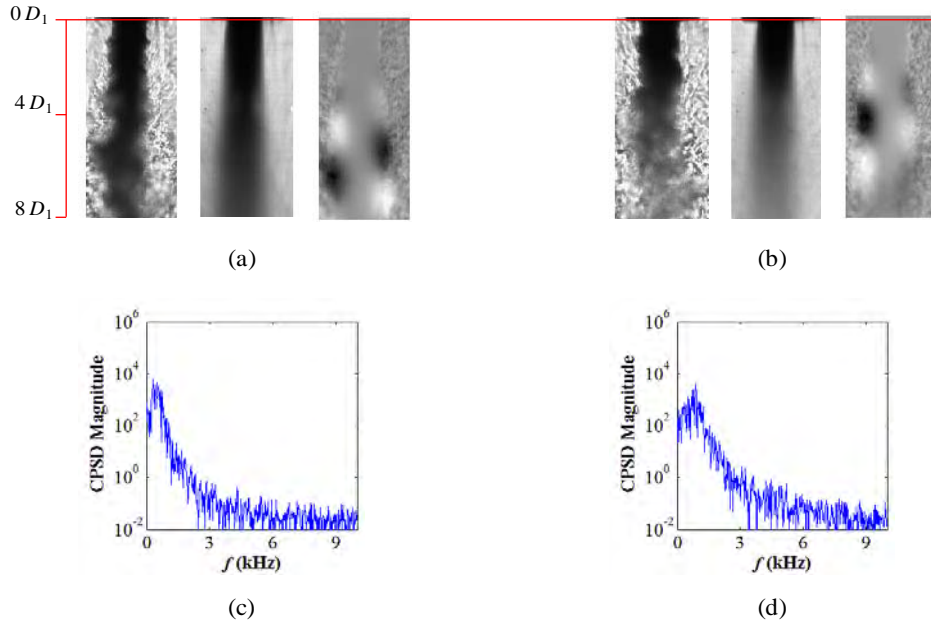
Figure 9. Baseline SAR flow at $Pr = 1.05$: snapshot, average, POM images for J (a) 9.4, (b) 19, and CPSD magnitude for J (c) 9.4, (d) 19.

ACOUSTICALLY FORCED (PAN)

The PAN condition established a region of locally maximum pressure fluctuation in the vicinity of the coaxial jets so that the velocity fluctuation was minimum or non-existent in the ideal case. As pressure is a scalar physical quantity, PAN can essentially be regarded as a condition that creates a symmetric fluctuation in pressure about the jet center plane that is normal to the transverse direction of propagation of the acoustic waves.

Figure 10 shows the flow response under PAN condition for the same case in Figure 3 without acoustics. The snapshot image in Figure 10(a) clearly depicts a series of orderly structures formed along almost the entire inner jet column. They appear to have started forming near the injector exit, and grew as they propagated farther downstream due to the entrainment effect of the outer jet. This planar view of the structures depicts them as varicose instability structures in a planar jet. As a matter of fact, varicose instability plays a similar role in planar jets as does axisymmetric instability in round jets [21]. The POMs shown in Figure 10(c) give further evidence of the symmetric structures that started forming immediately downstream of the injector exit, and spread as they traveled downstream.
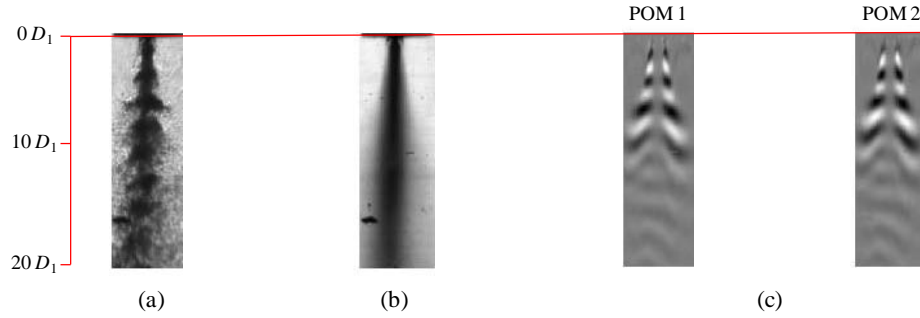
Figure 10. PAN forced (f_F = 3.14 kHz) LAR flow at Pr = 0.44, J = 0.5: (a) snapshot image, (b) average image, (c) proper orthogonal mode (POM).

The dark-core length and inner-jet spread angles also underwent noticeable changes under this forcing condition. The dark-core is visibly shorter ($< 20D_1$). As Figure 10(b) more vividly shows, on average, the dark-core flow pervades more of the flow field than it did in Figure 3(b), hence, indicating an enhanced mixing between the two flows.
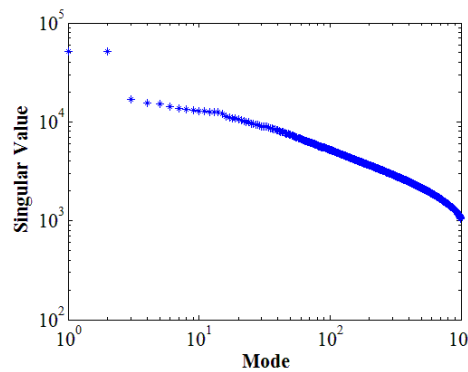
Figure 11. PAN forced (f_F = 3.14 kHz) LAR flow at Pr = 0.44, J = 0.5: singular values

Another unique nature of the flow response to PAN forcing is depicted in Figures 11 and 12(a, b). Figure 11 shows that the flow response to PAN forcing represented by POMs 1 and 2 in Figure 10(c) was the dominant type of response. The relative magnitudes of all other modes were similar to those for the baseline shown in Figure 4. Moreover, the spectral plots in Figures 12(a, b) associated with POMs 1 and 2 indicate that the orderly structures had a characteristic frequency that was identical to the forcing acoustic frequency, f_F. This may seem to be

a trivial outcome of external forcing, yet it does tell a lot about the nature of the flow stability as will be discussed below. Figure 12(c) shows the CPSD magnitude of the forced conjugate modes overlaid with the one for the baseline conjugate modes in Figure 5(c). It shows that f_F completely overtook the baseline characteristic frequencies, which are no longer visible in the spectra of the PAN condition.
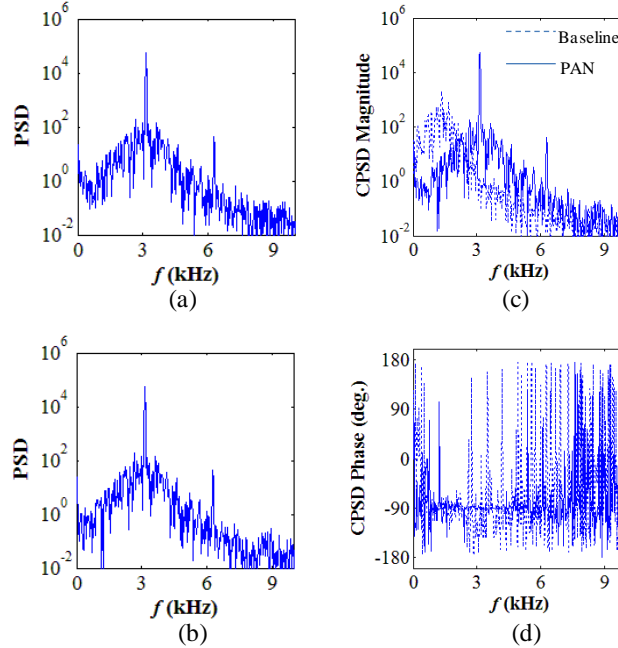

Figure 12. PAN forced ($f_F = 3.14$ kHz) LAR flow at $Pr = 0.44$, $J = 0.5$: power spectral density (PSD) of the temporal amplitude coefficients of the decomposition corresponding to (a) POM 1, (b) POM 2, and cross-power spectral density (CPSD) (c) magnitude, (d) phase.

Figures 13 and Figures 14 present the forced counterparts to the baseline cases at $Pr = 0.44$ and $Pr = 1.05$, respectively, presented in Figures 6 and 7 for varying J values using LAR. Similar to the forced case of $J = 0.5$ at $Pr = 0.44$, the forced lower J cases underwent noticeable reductions in their dark-core lengths while it became less and less so with increasing J as shown in Figures 13(a-d) and 14(a-d). In addition, for a similar J, it can be qualitatively argued that the $Pr = 1.05$ cases underwent a larger reduction in dark-core length compared to their $Pr = 0.44$ counterparts. The same argument involving surface tension or the lack there of can be made here as to why the $Pr = 1.05$ cases were more influenced by forcing.

The lobe patterns visible in the POMs also showed a peculiar transition with increasing J at both Pr conditions. Considering $Pr = 0.44$, for example, the lower J values [Figures 10(c) and 13(a)] showed a symmetric lobe pattern due to PAN forcing, whereas with increasing J, the symmetry became more skewed, and eventually turned into an antisymmetric pattern identical to the baseline cases. As noted earlier, antisymmetric pattern is the two-dimensional representation of a helical disturbance. The same trend was observed at $Pr = 1.05$. Thus, for the LAR geometry, it can be concluded that the dominant flow response to PAN forcing at low J is in the form of amplified symmetric disturbances, while that at higher J transitions to helical disturbances identical to those present in flows without acoustic forcing.
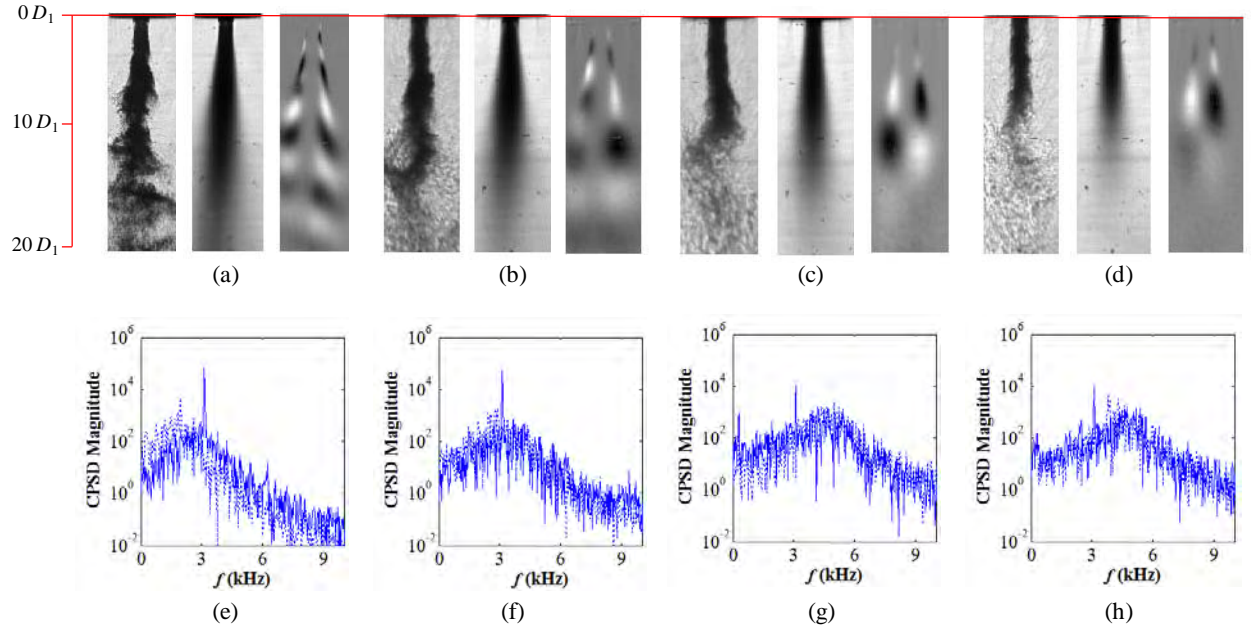
Figure 13. PAN forced LAR flow at $Pr = 0.44$: snapshot, average, POM images and CPSD magnitudes for J (a),(e) 2.1 ($f_F = 3.12$ kHz); (b),(f) 5.2 ($f_F = 3.12$ kHz); (c),(g) 11 ($f_F = 3.10$ kHz); (d),(h) 20 ($f_F = 3.11$ kHz). (·········· Baseline, ——— PAN)
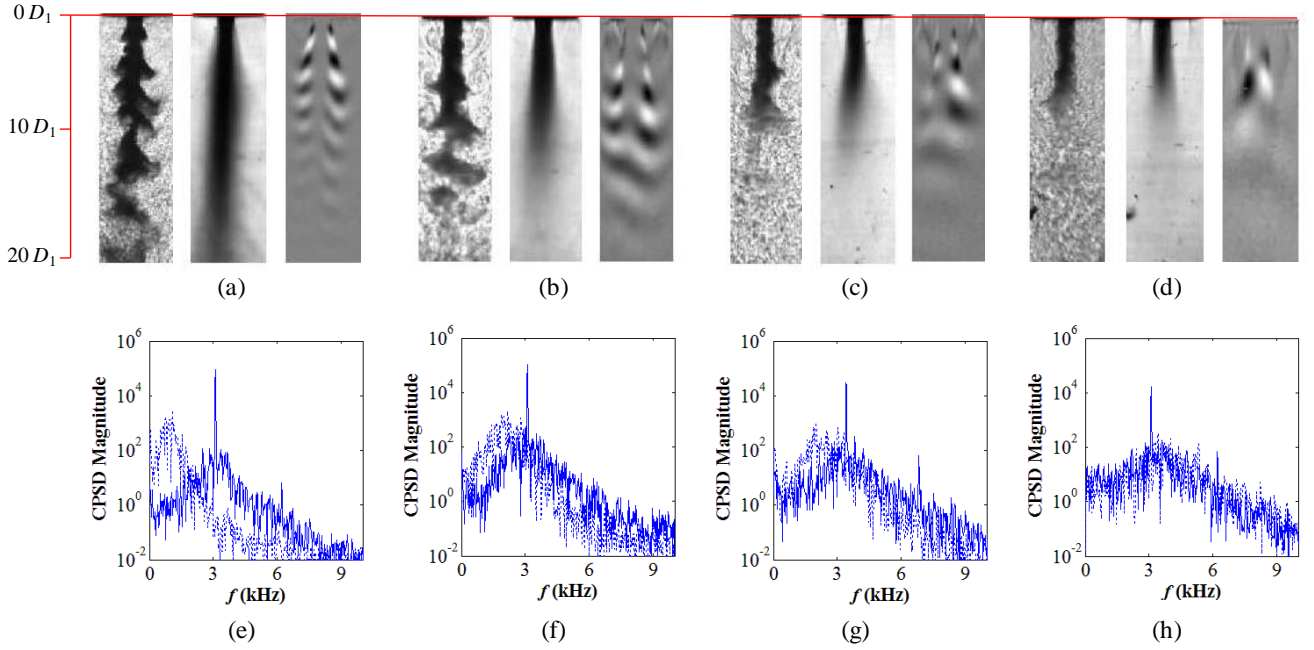

Figure 14. PAN forced LAR flow at $Pr = 1.05$: snapshot, average, POM images and CPSD magnitude for J (a) 0.5 ($f_F = 3.10$ kHz), (b) 1.9 ($f_F = 3.10$ kHz), (c) 5.0 ($f_F = 3.41$ kHz), (d) 12 ($f_F = 3.10$ kHz). (·········· Baseline, ——— PAN)

The temporal characteristics of the flow response to the acoustic forcing are shown in the spectral plots in Figures 13(e-h) and Figures 14(e-h) overlaid with the baseline spectra. Again considering $Pr = 0.44$, the spectral content of the lower J values [Figures 11(c) and 13(e)] was such that during forcing, a peak in the magnitude at f_F completely took over the low peak frequencies of the baseline flows. As J increased, the significance of the peak at f_F relative to the baseline peak frequencies became more and more diminished, and the forced spectra began retaining more of the baseline spectra, as clearly evident in the highest J attained (due to limitations of the experiment for the specified jet temperatures) in Figure 13(h). In other words, the spectral energy contained at f_F for lower J values was less so at higher J values. A similar trend in the spectra was also seen at $Pr = 1.05$, despite the highest attainable J was not as high as that for $Pr = 0.44$.

The nature of the flow response to an external disturbance depending on the flow condition, namely J, may be used to characterize the state of stability of the flow. Previous works [18,19,20] on flow stability characterize convectively unstable flows as noise amplifiers; that is, they are prone to external flow disturbances such as acoustic disturbances used in this study. Their spectral characteristics are such that when exposed to external forcing, their natural instabilities are completely removed and replaced by instabilities whose frequency match those of the forcing frequency [22]. Absolutely unstable flows, on the other hand, are characterized as naturally self-excited flows that do not respond well to external disturbances. Their spectra preserve the natural instabilities with or without a coexisting frequency content associated with the forcing frequency. These and the flow responses observed at both $Pr = 0.44$ and $Pr = 1.05$ may be used to argue that LAR flows may be characterized as convectively unstable for low J flows, and transition into absolutely unstable flows with increasing J values.

The response of SAR flows to PAN forcing were drastically different from that of LAR as shown in Figures 15 and Figures 16. At $Pr = 0.44$ and for lower J values ($J = 2.0$, 5.2), strong symmetric disturbances annihilate the inner jet flow, thus severely limiting the dark-core region to within 2-3D_1. The corresponding CPSD magnitude spectra also reveal local peaks around subharmonic frequencies ($0.5f_F$), which indicate vortex merging processes. For the higher J values ($J = 12$, 17), although symmetric disturbances were not as strong as in the lower J cases, they nevertheless were still prevalent as evident in the POM images and the CPSD magnitude spectra. At $Pr = 1.05$, symmetric disturbances were again prevalent even for the highest J. However, as their spectra reveals, disturbances at the subharmonic frequencies were the most dominant indicating that vortex merging prevailed in the flow field.
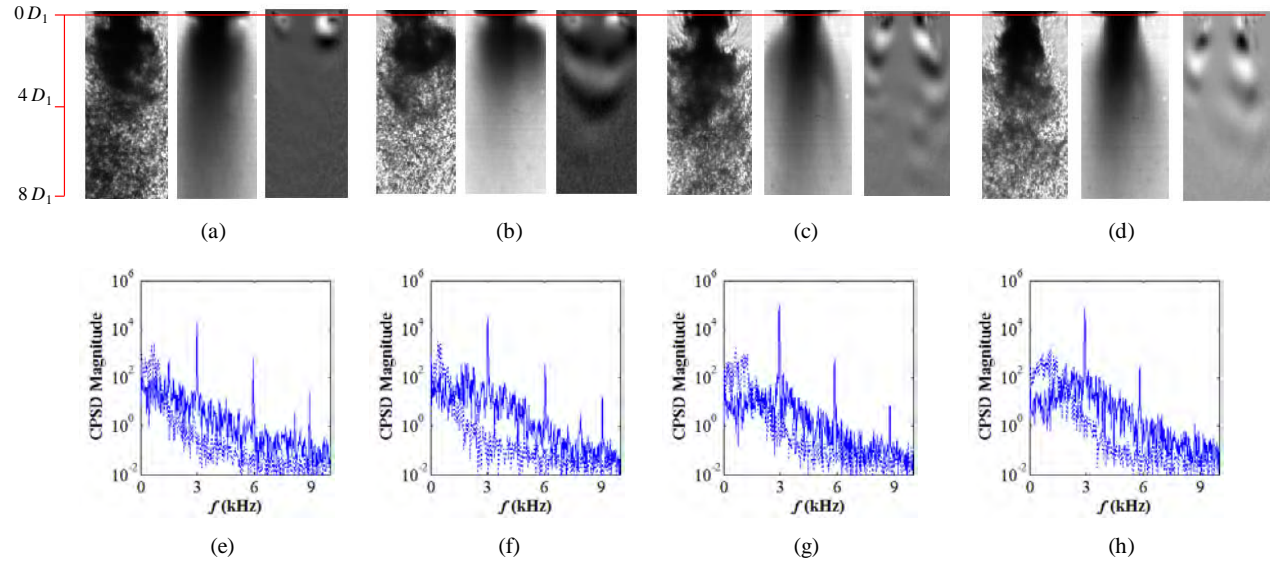

Figure 15. PAN forced SAR flow at $Pr = 0.44$: snapshot, average, POM images and CPSD magnitude for J (a),(e) 2.0 ($f_F = 2.97$ kHz); (b),(f) 5.2 ($f_F = 3.02$ kHz); (c),(g) 12 ($f_F = 2.92$ kHz); (d),(h) 17 ($f_F = 2.90$ kHz). (·········· Baseline, ——— PAN)

As the spectra in Figures 15(e-f) and Figures 16(c, d) also reveal, the flow showed strong response to external forcing regardless of the *J* value. This was again evident by the lack of any remnants of the low-frequency peaks present in the forced spectra. Accordingly, SAR flows depicted the behavior of convectively unstable flows per the discussion for LAR.
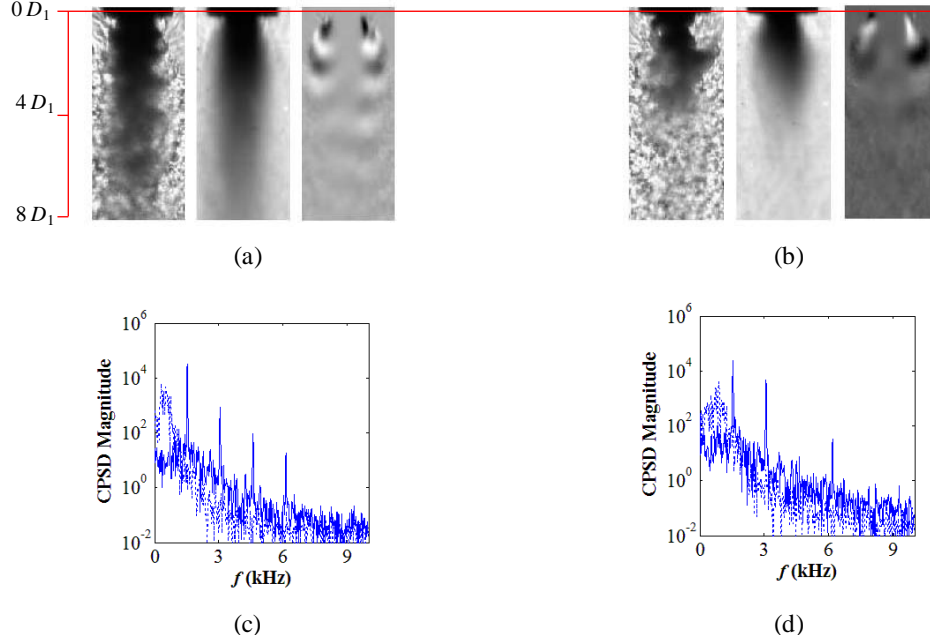

(a)   (b)

(c)   (d)

Figure 16. PAN forced SAR flow at *Pr* = 1.05: snapshot, average, POM images and CPSD magnitude for *J* (a),(c) 9.4 (f_F = 3.07 kHz); (b),(d) 19 (f_F = 3.09 kHz). (·········· Baseline, ——— PAN)

From a practical standpoint, it is crucial to ensure that the injector flow under non-design operating conditions behave as closely as possible to that under design operating conditions. Flow disturbances that arise as a result of acoustic instabilities due to excitation of the combustion chamber acoustic modes are typical instances of non-design operating conditions. Although special cases of the chamber acoustic behavior can be modeled and incorporated in the design considerations, a great many other unpredictable scenarios exist. Hence, the best approach is to implement a robust design that guarantees predictable flow behavior for a given set of flow conditions regardless of any externally imposed disturbances. In light of this argument, LAR would be considered a preferable design configuration solely on the fact that it has been shown to be less sensitive to external disturbances at high *J* values.

CONCLUSION

This study examined the dynamic behavior of flow structures that develop in the inner shear layer of shear-coaxial nonreactive jets with and without the present of transverse acoustic forcing. A proper orthogonal decomposition of pixel intensity fluctuation data revealed both the spatial and temporal characteristics of these flow structures for subcritical and nearcritical pressure regimes and a range of *J* values using two injector exit geometries.

The large outer-to-inner jet area ratio (LAR) injector baseline flows exhibited helical instabilities at far enough downstream locations regardless of *J*. The frequencies of the flow structures associated with these helical instabilities shifted to higher frequencies with increasing magnitudes of jet velocities. Pressure antinode (PAN) acoustic forcing of low *J* LAR flows showed strong response by forming symmetric structures whose frequencies were identical with the forcing frequencies. Magnitude spectral plots also showed large peaks at the forcing frequencies and the baseline flow peak frequencies were completely removed from the forced spectra. With

increasing *J*, however, the response to forcing became gradually weaker, and the broad baseline peak frequencies coexisted with the peaks at the forcing frequency.

The small outer-to-inner jet area ratio (SAR) injector baseline flows also exhibited helical instabilities. However, unlike LAR, the frequencies of the flow structures did not show significant shift to higher frequencies with increasing jet velocities. In addition, regardless of *J*, they showed strong response to PAN forcing. Thus, due to their readily responsiveness to external acoustic forcing, SAR flows may be regarded as a class of flows that display convectively unstable behavior. On the contrary, LAR flows displayed a transition from convectively unstable to absolutely unstable flow behavior with increasing *J*. This makes LAR flows at large enough *J* more desirable from a design standpoint since they behave in a predictable manner despite externally imposed disturbances such as those that arise due to the excitation of combustion chamber acoustic modes.

REFERENCES

[1] Ko, N. W. M. and Kwan, S. H. 1976 The initial region of subsonic coaxial jet. *J. Fluid Mech.* **73**, 305-332.

[2] Dahm, W. J. A., Frieler, C.E., and Tryggvason, G. 1992 Vortex structure and dynamics in the near field of a coaxial jet. *J. Fluid Mech.* **241,** 371-402.

[3] Wicker, R.B. and Eaton, J.K. 1994 Near Field of a Coaxial Jet With and Without Axial Excitation. *AIAA Journal* **32**, 542-546.

[4] Balarac, G., Métais, O. and Lesieur, M. 2007 Mixing enhancement in coaxial jets through inflow forcing: A numerical study. *Phys. Fluids* **19**, 075102.

[5] Gladnick, P. G., Enotiadis, A. C., LaRue, J. C. and Samuelsen, G. S. 1990 Near-feld characteristics of a turbulent coflowing jet. *AIAA Journal* **28**, 1405-1414.

[6] Cohen, J. and Wygnanski, L. 1987 The Evolution of Instabilities in an Axisymmetric Jet, Part I. Linear Growth of Disturbances Near the Nozzle. *J. Fluid Mech.* **176**, 191-219.

[7] Michalke, A. and Hermann, G. 1982 On the inviscid instability of a circular jet with external flow. *J. Fluid Mech.* **114**, 343-359.

[8] Davis, D.W., "On the behavior of a shear-coaxial jet, spanning sub- to supercritical pressures, with and without an externally imposed transverse acoustic field. Ph.D. Thesis," Penn State University, 2005.

[9] Davis, D.W. and Chehroudi, B. 2007 Measurements in an Acoustically Driven Coaxial Jet under Sub-, Near-, and Supercritical Conditions. *J. Propulsion and Power* **23**, 2.

[10] Leyva, I. A., Chehroudi, B., Talley, D., "Dark-core analysis of coaxial injectors at sub-, near-, and supercritical conditions in a transverse acoustic field", *54th JANNAF Meeting*, Denver, CO, May 14-18, 2007

[11] Leyva, I.A., Chehroudi, B. and Talley, D., "Dark-core analysis of coaxial injectors at sub-, near-,and supercritical pressures in a transverse acoustic field". *43rd AIAA/ASME/SAE/ASEE Joint Propulsion Conference and Exhibit*, AIAA 2007-5456.

[12] Leyva, I.A., Rodriguez, J.I., Chehroudi, B. and Talley, D. Preliminary, "Results on Coaxial Jet Spread Angles and the Effects of Variable Phase Transverse Acoustic Fields. *46th AIAA Aerospace Sciences Meeting and Exhibit*, AIAA 2008-950.

[13] Rodriguez, J. I., Graham, J. J., Leyva, I. A., Lyu, H.-Y., Talley, D., "On the Inner Jet Spread Angles of Coaxial Jets from Subcritical to Supercritical Conditions with Preliminary Numerical Results", *55th JANNAF Propulsion/4th Liquid Propulsion Subcommittee Meeting*, Orlando, FL, December 8-12, 2008.

[14] Rodriguez, J. I., "Acoustic Excitation of Liquid Fuel Droplets and Coaxial Jets," Ph.D. Thesis, University of California, Los Angeles, 2009.

[15] Chatterjee, A. 2000 An introduction to the proper orthogonal decomposition. *Current Science* **78**, 7.

[16] Arienti, M, and Soteriou, M.C. 2009 Time-resolved proper orthogonal decomposition of liquid jet dynamics. *Phys. Fluids* **21**, 112104.

[17] Narayanan,V., Lightfoot, M.D.A, Schumaker, S.A. Schumaker, Danczyk, S.A., and Eilers, B., "Use of Proper Orthogonal Decomposition Towards Time-resolved Image Analysis of Sprays," *ILASS Americas, 23rd Annual Conference on Liquid Atomization and Spray Systems*, Ventura, CA, May 2011

[18] Huerre, P. and Monkewitz, P.A. 1990 Local and Global Instabilities in Spatially Developing Flows. *Annu. Rev. Fluid Mech.* **22,** 473-537

[19] Huerre P. 2000. Open shear flow instabilities. In *Perspectives in Fluid Dynamics*, ed. G.K. Batchelor, H.K. Moffatt, M.G. Worster, pp. 159–229. Cambridge, UK: Cambridge Univ.

[20] Jendoubi, S. and Strykowski, P.J. 1994 Absolute and convective instability of axisymmetric jets with external flow. *Phys. Fluids* **6**, 3000.

[21] Sevilla, A., Gordillo, J. M. and Martínez-Bazán, Ç. 2002 The effect of the diameter ratio on the absolute and convective instability of free coflowing jets. *Phys. Fluids* **14**, 3028.

[22] Megerian, S., Davitian, J., Alves, L. S. de B. & Karagozian, A. R. 2007 Transverse jet shear-layer instabilities. Part 1. Experimental studies. *J. Fluid Mech.* **593**, 93–129.

APPENDIX

Table 2. Summary of flow conditions and parameters

Pr = 0.44, LAR

J	R	$T_{chamber}$ (K)	$\rho_{chamber}$ (kg/m^3)	$P_{chamber}$ (MPa)	T_{outer} (K)	$\dot{m}_{outer}$ (mg/s)	ρ_{outer} (kg/m^3)	u_{outer} (m/s)	Re_{outer} (10^4)	T_{inner} (K)	$\dot{m}_{inner}$ (mg/s)	ρ_{inner} (kg/m^3)	u_{inner} (m/s)	Re_{inner} (10^4)
0.5	3.5	217	24	1.50	204	1106	26	10.7	3.1	110	727	622	3.0	2.4
2.1	7.4	220	23	1.50	205	2212	25	21.5	6.3	107	725	646	2.9	2.1
5.2	11	221	23	1.50	203	3531	26	33.9	10	108	733	639	3.0	2.2
11	17	216	24	1.51	204	4991	26	47.9	14	107	722	646	2.9	2.1
20	22	220	23	1.50	204	4633	26	44.8	13	110	482	622	2.0	1.6

Pr = 1.05, LAR

J	*R*	$T_{chamber}$ (K)	$\rho_{chamber}$ (kg/m³)	$P_{chamber}$ (MPa)	T_{outer} (K)	$\dot{m}_{outer}$ (mg/s)	ρ_{outer} (kg/m³)	u_{outer} (m/s)	Re_{outer} (10⁴)	T_{inner} (K)	$\dot{m}_{inner}$ (mg/s)	ρ_{inner} (kg/m³)	u_{inner} (m/s)	Re_{inner} (10⁴)
0.5	2.1	223	56	3.56	199	1742	65	6.6	4.8	115	724	605	3.1	2.5
1.9	4.1	221	57	3.56	200	3479	65	13.3	9.6	118	724	577	3.3	2.8
5.0	6.5	223	57	3.58	203	4189	64	16.2	11	122	511	531	2.5	2.4
12	9.9	223	56	3.57	208	6217	62	24.9	17	124	482	497	2.5	2.5

Pr = 0.44, SAR

J	*R*	$T_{chamber}$ (K)	$\rho_{chamber}$ (kg/m³)	$P_{chamber}$ (MPa)	T_{outer} (K)	$\dot{m}_{outer}$ (mg/s)	ρ_{outer} (kg/m³)	u_{outer} (m/s)	Re_{outer} (10⁴)	T_{inner} (K)	$\dot{m}_{inner}$ (mg/s)	ρ_{inner} (kg/m³)	u_{inner} (m/s)	Re_{inner} (10⁴)
2.0	6.9	246	21	1.49	195	450	27	6.6	1.1	109	925	630	0.96	1.5
5.2	11	217	24	1.49	184	750	29	10	1.9	110	925	620	0.97	1.5
12	17	222	23	1.49	194	1100	27	16	2.6	108	925	640	0.94	1.4
17	20	217	24	1.48	194	1300	27	19.3	3.1	108	925	638	0.95	1.4

Pr = 1.05, SAR

J	*R*	$T_{chamber}$ (K)	$\rho_{chamber}$ (kg/m³)	$P_{chamber}$ (MPa)	T_{outer} (K)	$\dot{m}_{outer}$ (mg/s)	ρ_{outer} (kg/m³)	u_{outer} (m/s)	Re_{outer} (10⁴)	T_{inner} (K)	$\dot{m}_{inner}$ (mg/s)	ρ_{inner} (kg/m³)	u_{inner} (m/s)	Re_{inner} (10⁴)
9.4	9.9	214	59	3.58	203	1460	63	9.2	3.2	109	925	650	0.93	1.3
19	14	215	59	3.56	207	2060	62	13	4.5	111	925	635	0.95	1.4